Development of Fe-9Cr Alloy via High-Energy Ball Milling and Spark Plasma Sintering

Chao Jiang, Anumat Sittiho, Arnab Kundu, Indrajit Charit, Brian Jaques

May 2019

INL

Idaho National Laboratory

The INL is a U.S. Department of Energy National Laboratory operated by Battelle Energy Alliance

Development of Fe-9Cr Alloy via High-Energy Ball Milling and Spark Plasma Sintering

Chao Jiang, Anumat Sittiho, Arnab Kundu, Indrajit Charit, Brian Jaques

May 2019

Idaho National Laboratory
Idaho Falls, Idaho 83415

http://www.inl.gov

Development of Fe-9Cr Alloy via High-Energy Ball Milling and Spark Plasma Sintering

Arnab Kundu[a], Anumat Sittiho[a], Indrajit Charit[a,1], Brian Jaques[b], and Chao Jiang[c]

[a] Department of Chemical and Materials Engineering, University of Idaho, Moscow, ID

[b] Department of Material Science and Engineering, Boise State University, Boise, ID

[c] Idaho National Laboratory, Idaho Falls, ID

Abstract

Iron and chromium powders were mixed and mechanically alloyed via high-energy ball milling for different time durations (2–20 h) to produce an alloy powder with a nominal composition of Fe-9Cr (wt.%). The milled Fe-9Cr powders were analyzed using scanning electron microscopy (SEM), x-ray diffraction (XRD) and transmission electron microscopy (TEM) to understand the impact of ball milling (BM) time on the characteristics of the milled powder. The optimized milled powder samples were then consolidated via spark plasma sintering (SPS) for different dwell times and temperatures. The density of consolidated samples was found to reach a maximum of 98%. Microstructural characterization of the SPS samples were performed using XRD, SEM, TEM and electron backscatter diffraction. This study highlights the principles and importance of high-energy BM and SPS of Fe-9Cr model alloy for the future development of more complex oxide dispersion-strengthened alloys for various applications including advanced nuclear reactor applications.

Keywords: High energy ball milling, Fe-Cr, XRD, SEM

1. Introduction

High-chromium (9–14 wt.%) alloys are favorable for future sodium fast reactor fuel cladding materials,1,2,3 which require high-radiation swelling resistance and resistance to attack from liquid sodium.4 Oxide dispersion strengthened (ODS) steels based on Fe-(9-14)% Cr alloys are quite promising for such applications. Generally, the processing routes for fabricating such alloys involve mechanical alloying MA which incorporates rare earth oxides in the Fe-Cr matrix. MA is a processing method that involves repeated fracturing, welding and re-fracturing of a mixture of powder particles to produce a controlled, extremely fine microstructure which cannot be easily produced via conventional ingot metallurgy. The milled powder is consolidated into bulk shapes and heat-treated to obtain the desired

---

[1] Corresponding author. I. Charit; e-mail: icharit@uidaho.edu, phone: 208-885-5964, fax: 208-885-7462

characteristics.[5] It has been reported that the morphology, grain size distribution and contamination of the milled powders strongly depend on the process variables of MA such as milling time, process control agent, ball-to-powder weight ratio, milling atmosphere, etc.[6,7,8,9,10,11] Formation of nanostructures during milling has been established as one of the most effective mechanism to increase solid solubility due to a higher fraction of atoms at the grain boundaries and an enhanced diffusion path.[12]

Spark plasma sintering (SPS) is a thermal and pressure-assisted compaction/sintering process. It is also known as the field-assisted sintering technique (FAST)[13] or pulsed electric current sintering.[14] This process utilizes a combined action of a pulsed direct electrical current and pressure to perform high-speed consolidation of the powder. The direct method of heating allows for very high heating rates, thus increasing densification due to enhanced diffusion.[15,16,17] It is regarded as a rapid sintering method in which the heat is distributed over the volume of the powder compact and dissipates exactly at the contact points of the powder particles. SPS systems offer many advantages over conventional techniques such as hot pressing, hot isostatic pressing (HIP) or pressureless sintering, including the ease of operation and accurate control of sintering energy, resulting in lower-temperature sintering and less time, and applicability to both electrically conductive and non-conductive materials.

The Fe-9Cr alloy serves as a base matrix for the Fe-9Cr ODS alloy which has attracted much interest.[18,19] Even though higher-Cr ODS alloys have better corrosion/oxidation resistance, they often suffer from thermal aging embrittlement and irradiation embrittlement because of alpha-prime phase formation.[20] However, Fe-9Cr-based ODS steels are relatively free from such effects because of their lower Cr content. Thus, it is important to understand the Fe-9Cr matrix behavior. Fe-9Cr alloy has been primarily made by casting,[21,22] but only limited work has been reported on the powder metallurgy-sourced Fe-9Cr alloy. Heintze et al.[23] conducted high-energy ball milling (BM) followed by SPS and HIP. The present work was taken up to gain an understanding of the effects of the BM and SPS parameters on the microstructure and morphological characteristics and the mechanical properties of Fe-9Cr alloy. An effort has also been made to understand the SPS kinetics.

Materials and Methods

Iron powder (99.9 + % metal basis) of around 10 μm size and chromium powder (99.95% metal basis) of 50 μm size were mixed in ratio of 91:9, respectively, and poured into a stainless steel vial without any surfactant along with stainless steel balls (milling medium) of 8 mm diameter inside an argon atmosphere-controlled glove box to prevent

oxidation/contamination. The ball-to-powder weight ratio was around 10:1.24 About half of the steel vial was empty after the mixture of powder and steel balls was poured. The filled vials were loaded into a shaker mill (SPEX 8000 M) and milled for various durations (2 h, 5 h, 8 h, 10 h, 12 h, 15 h, and 20 h). The carbon and nitrogen content of the powders were found to be approximately 0.02 wt.% and 0.024 wt.%, respectively, estimated using combustion analysis. The chromium content of the 10-h ball-milled sample was estimated by inductively coupled plasma test and found to be 8.97 wt.% which is essentially the target composition (i.e., 9 wt.% Cr).

The milled powders were characterized in Zeiss Supra 35 VP field-emission gun scanning electron microscope to examine the powder size and morphology. x-ray diffraction (XRD) of the ball-milled powders was performed using a Siemens 5000D diffractometer with CuKα x-ray radiation (wavelength, 0.1541 nm). Modifications such as adaptive smooth, kα2 Rachinger and background correction by the Sonnerveld method were applied to the XRD patterns using Powder–X software. From the XRD data, the lattice parameter of the milled powders was calculated based on the Nelson–Riley relationship.25 The crystallite size and lattice strain were evaluated using the Williamson–Hall equation26:

$$\beta_{hkl} = 0.94(l/L\cos\theta_{hkl}) + 4\varepsilon\tan\theta_{hkl}$$

$$(1)$$

where β_{hkl} is the full width half maxima of the XRD peak, $2\theta_{hkl}$ is the diffraction angle, L is the crystallite size and ε is the lattice strain. Transmission electron microscopy (TEM) was performed in a JEOL 2010J TEM at an accelerating voltage of 200 kV to study the inherent structure of the 10-h milled powder.

A Dr. Sinter Lab SPS-515S (SPS Syntex, Kanagawa, Japan) available at the Center for Advanced Energy Studies, Idaho Falls, USA, was used to consolidate the milled powder. A Tri-Gemini cylindrical graphite die with an inner diameter of 12.7 mm and outer diameter of 38 mm was used. The inner surface of the die was covered with a graphite foil with a thickness of 0.25 mm to facilitate sample removal. The milled powder was cold-compacted inside the graphite die, and a 0.2-mm-thick graphite foil was placed between the powder and transmission electron microscopy punches. The die was wrapped in a 4-mm-thick layer of graphite felt to minimize heat loss by thermal radiation. Degassing was performed by continually purging with argon gas and pumping the chamber down to 9.33×10^{-7} MPa, and repeated at least thrice before starting the sintering process. The milled powder batches were

heated in the vacuum chamber to four different temperatures (850°C, 950°C, 1000°C, and 1050°C) at a rate of 100°C/min and then held for 7 min, 15 min, 30 min, and 45 min. The temperature was monitored with a K-type thermocouple inserted through a hole in the die. A constant uniaxial pressure of 80 MPa was applied to the milled powder during SPS. The samples were then cooled to room temperature in the SPS chamber at 50°C/min. The final product was in the form of a disk with dimensions of 12.5 mm diameter and 4.8 mm thickness.

The density of the sintered samples was measured by Archimedes principle. The weight of the samples was taken in air and in fully immersed condition in deionised water using an Ohaus Precision Balance (HRB-200). The density of deionised water (1 g/cm3) and the density of air (0.0012 g/cm3) at standard room temperature and pressure were used for density calculations. The theoretical density was taken to be around 7.81 g/cm3. The relative density was estimated in terms of the percentage of theoretical density.

Vickers microhardness tests were performed using LECO 100 M microhardness tester at a load of 0.5 kg and a loading time of 15 s at 10 different random points. All Vickers hardness numbers (VHN) reported in this study are given in the units of kgf/mm2. The same x-ray diffractometer and TEM were used for analyzing the phase constituents and grain size of the SPS samples. For preparing the TEM specimens, an electro-jet polishing technique was used. A solution of CH3OH-HNO3 (80:20, by vol.%) was used as electrolyte at -40°C and a voltage of 25 V using a Fischione Model 110 Twin-Jet Electropolisher. Electron backscatter diffraction (EBSD) analysis was carried out with a Thermoscientific Quasor™ system available in a scanning electron microscopy (SEM) at an accelerating voltage of 20 kV and at a 70° tilt angle having a resolution of 2 pixels × 2 pixels. Compression testing was performed at room temperature under a strain rate of 10^{-3} s^{-1} using an Instron 5982 universal tester.

Results and Discussion

Microstructural Characteristics of the Milled Fe-9Cr Powders

The milled powder batches were examined by SEM and TEM (Fig. 1). Figure 1a, b, and c shows the representative SEM images of the powder samples ball-milled for 2 h, 10 h, and 20 h, respectively. Powder size analysis revealed that the mean powder size decreased with increasing milling time, as shown in Fig. 1f. Also, it can be noted that the powder size distribution became progressively narrower with increasing milling time. Due to continuous collision of the powder particles with the balls, the powder particles break down into smaller

particles. As seen in Fig. 1a, the mean powder size was around 50 ± 20 μm for the powder ball-milled for 2 h. With continued deformation, the powder particles are work-hardened and fractured by fatigue failure or impact fragmentation,[27] and the minimum powder size is found to be 15 μm. Figure 1d shows a bright field TEM image while the corresponding selected area diffraction (SAD) pattern of the milled powder is shown in Fig. 1e. The microstructure shows a uniform distribution of nanograins. The crystallite size measurement was carried out using the mean linear intercept method and the average grain size was measured to be around 12 nm, which is consistent with the crystallite size determined from the XRD data (11.3 nm). The rings in the SAD pattern are from the ferritic matrix phase and no diffraction from any other phases is observed.[28]
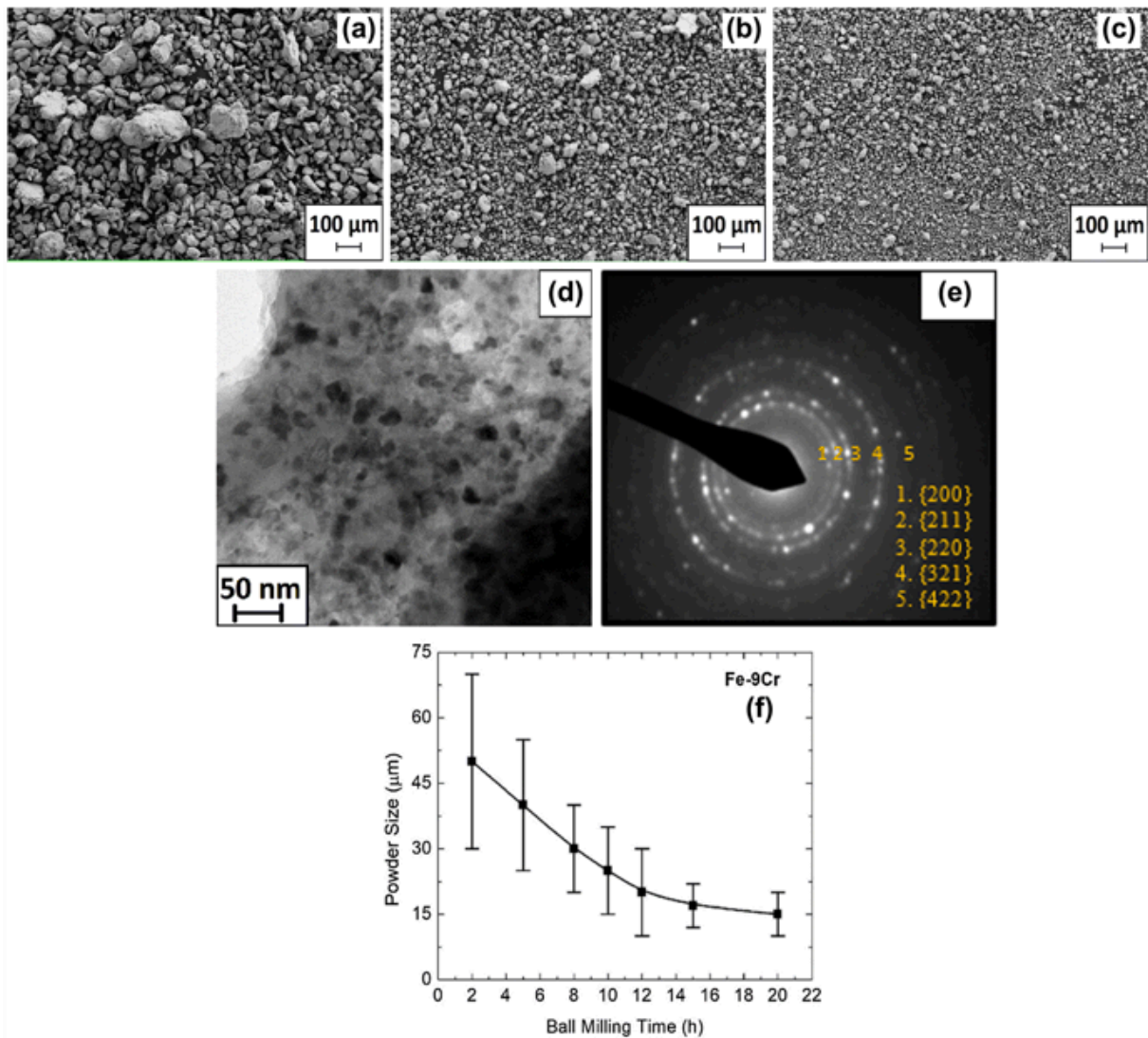

Fig. 1
Secondary electron SEM images of Fe-9Cr powders milled for various time periods: (a) 2 h, (b) 10 h, (c) 20 h. TEM image of (d) 10-h milled and (e) SAD pattern of the 10-h milled powder at 300 mm camera length. (f) Variation of powder size as a function of milling time.

Figure 2 shows the XRD patterns of the various milled powder samples. Prominent peaks are observed near the diffraction angles (2θ) of 44.91°, 65.46°, and 82.57°. These peaks correspond to the planes {110}, {200}, and {211} of ferrite (BCC), respectively.[29]
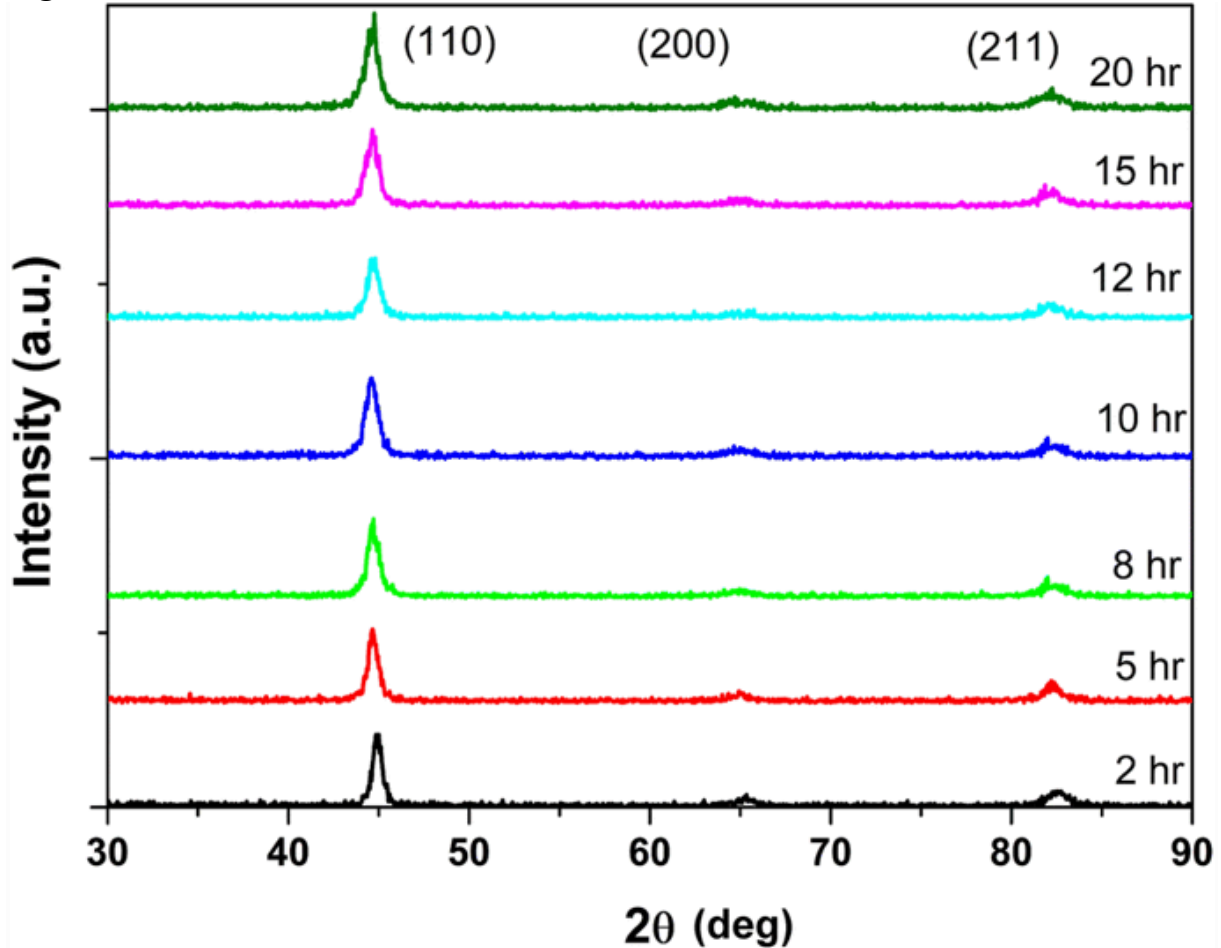
Fig. 2

Fig. 2
XRD patterns of Fe-9Cr powder batches milled for various durations

Broadening of the diffraction peaks is also observed with increasing milling time, which can be due to the introduction of strain and decrease of crystallite size of the powders.[30] A small shift of the peak positions toward the left is seen as a result of the solid solutionizing of Cr in Fe and increasing strain during milling.

Table I shows the variation of the lattice parameter, crystallite size and lattice strain with BM time. The lattice parameter on average is 2.880 ± 0.001 Å, which is inbetween those of iron (2.87 Å) and chromium (2.89 Å). According to Vegard's Law,[31] the lattice parameter of Fe-9Cr solid solution is 2.872 Å.

Table I. Lattice parameter, crystallite size and lattice strain of the Fe-9Cr powder batches ball-milled for various durations, as analyzed from the XRD data

Ball-milling time (h)	Lattice parameter (Å)	Crystallite size (nm)	Strain (%)
2	2.871±0.001	14.91±0.02	0.64±0.02
5	2.882±0.001	14.66±0.02	0.66±0.02
8	2.881±0.001	13.27±0.02	0.72±0.02
10	2.891±0.001	11.34±0.02	0.84±0.02
12	2.882±0.001	10.97±0.02	0.87±0.02
15	2.872±0.001	10.69±0.02	0.89±0.02
20	2.881±0.001	10.35±0.02	0.92±0.02

The crystallite size decreases with the increase in BM time. High-energy ball-milling being a severe plastic deformation process, the process introduces progressively higher amounts of strain leading to smaller crystallite size with increasing milling time.

Characteristics of Spark Plasma-Sintered Fe-9Cr Samples

Evaluation of Density and Microhardness

The variation of relative density of the sintered samples with sintering time is shown in Fig. 3a. Sintering was conducted for four different dwell times (7 min, 15 min, 30 min, and 45 min) at a constant temperature of 950°C and an applied pressure of 80 MPa. The density of the samples increases with increasing sintering time. The SPS process, being a diffusion-controlled process, allows prolonged duration of diffusion to take place resulting in a progressive decrease in porosity. However, the effect of sintering temperature is found to be more effective on densification. Figure 3b shows the variation of relative density of the sintered samples as a function of sintering temperature. There are four sintering temperatures (850°C, 950°C, 1000°C, and 1050°C), for which the sintering time and applied pressure were kept the same, i.e. 45 min and 80 MPa, respectively. With increasing sintering temperature, the relative density of the sintered samples increases. Given the diffusional nature of sintering, a higher temperature would lead to greater diffusivity leading to greater densification. However, at a higher sintering temperature (1050°C), there is a likelihood of additional pore formation due to spark discharge and other factors, which can lead to a slight decrease in density. The maximum density ($97.9 \pm 0.1\%$) is obtained for the sample sintered at 1000°C for 45 min.
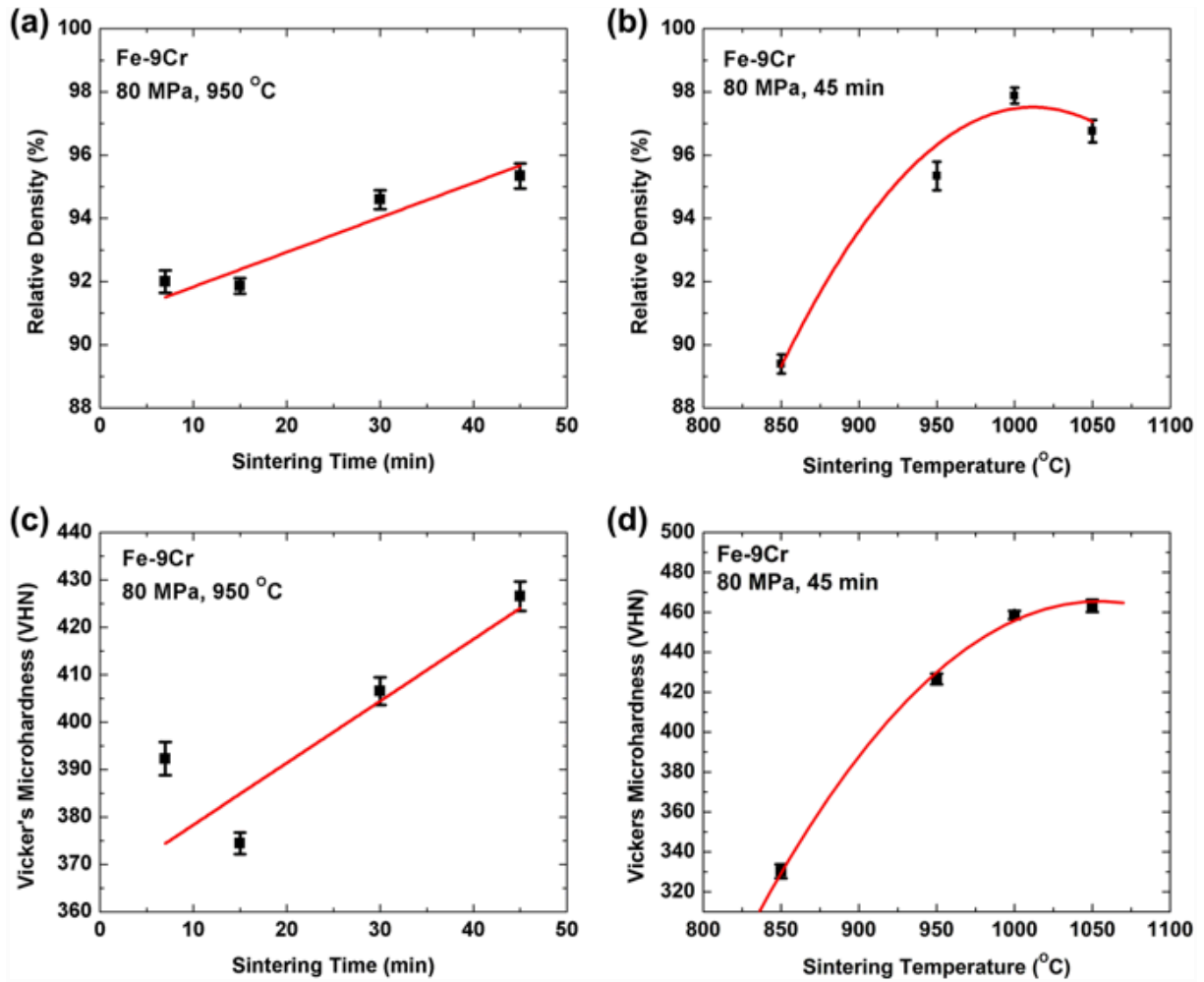
Fig. 3
The variation of relative density of sintered Fe-9Cr samples with (a) sintering time and (b) sintering temperature; and the variation of Vickers microhardness as a function of (c) sintering time and (d) sintering temperature

The microhardness of the samples was measured by Vickers microhardness testing. Figure 3c shows the variation of the microhardness of the samples with sintering time. Four sintering times (7 min, 15 min, 30 min, and 45 min) were selected, all of which were carried at a constant temperature of 950°C. The trend shows an increase in microhardness with increasing sintering time. The reason behind this is likely that, with increasing sintering time, the powder has more time to become densified because SPS is a diffusion-controlled process. Thus, with densification (i.e., a decrease in porosity) the hardness also increases. Figure 3d shows the variation of microhardness of the samples with sintering temperature. The four sintering temperatures were 850°C, 950°C, 1000°C, and 1050°C. The sintering time was 45 min and the sintering pressure was 80 MPa and were kept constant when operating at different temperatures. The analysis shows that there is an increasing trend in the hardness of the samples up to 1050°C. The process of densification, being diffusion-controlled, allows

the densification rate to increase and in turn increases the hardness. However, the rate of increase in hardness decreases considerably at 1050°C because of a combined effect of porosity generation and grain growth.

Microstructural Characteristics

Figure 4a–c shows the SEM imaging of the Fe-Cr samples. The specimen sintered at 850°C for 45 min yielded a low density and hardness compared to the others and so we did not carry out any SEM imaging for that sample. Grain size analysis carried out by the mean linear intercept method showed the average grain sizes to be 1.9 ± 1.0 μm, 2.0 ± 1.0 μm, and 2.5 ± 1.0 μm for the samples sintered for 45 min at 950°C, 1000°C, and 1050°C, respectively. Quantitative energy dispersive spectroscopy at various points on the sample showed the presence of Cr in the range of 9 ± 1 wt.%, which represents relatively homogeneous distribution of chromium throughout the matrix.
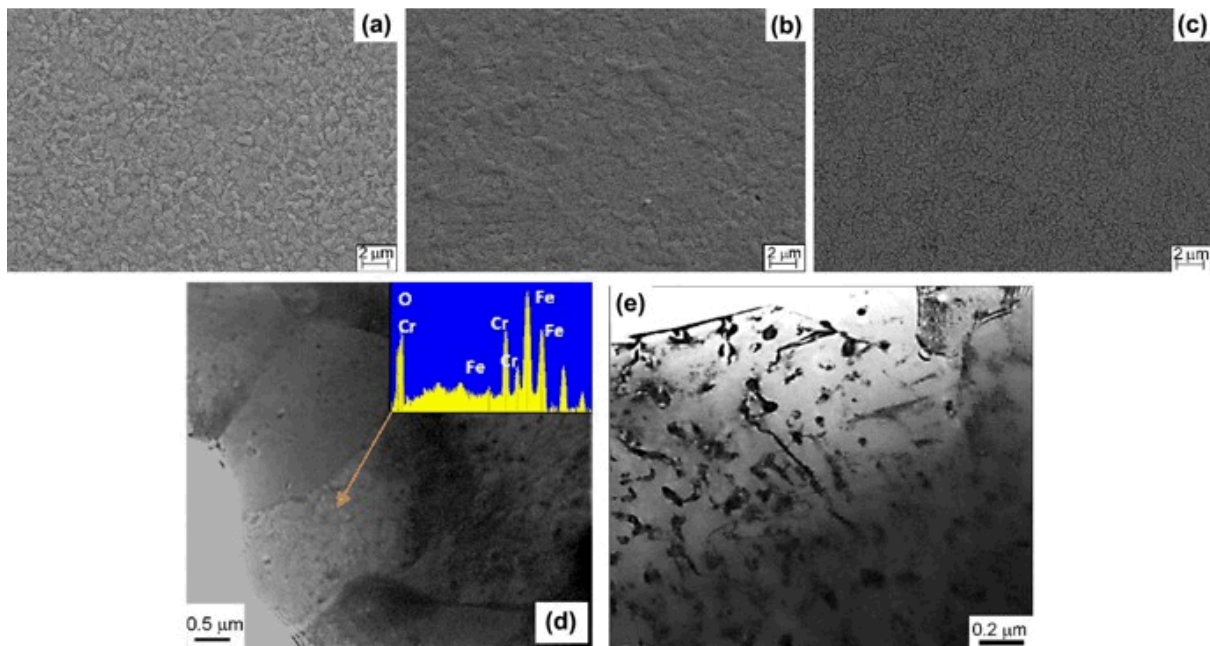

Fig. 4
Secondary electron SEM images of Fe-9Cr alloy specimens 10-h ball- milled and SPS for 45 min at (a) 950°C, (b) 1000°C, and (c) 1050°C. TEM images of 10-h BM and SPS for 45 min at (d) 950°C, and (e) 1000°C

Figure 4d and e shows the TEM images of the SPSed Fe-9Cr samples sintered at 950°C and 1000°C respectively. Some second phase particles are observed in the matrix. These particles nucleated during BM and undergrown growth during the SPS process. So, Fe-Cr alloy produced is not truly a single-phase solid solution alloy but rather a Fe-Cr matrix with Cr-based oxide phases. Note that earlier studies on pure iron undergoing high-energy ball-milling and SPS reported the formation of Fe-based oxide particles. Cr having more affinity

for oxygen compared to Fe helped in forming Cr oxides.32 Also, milling starting with the constituent powder along with some oxygen present already on the surface and ingress of oxygen from the milling environment can help form the precursors of these oxides and they became clearly resolvable in TEM after SPS.

The relative density of the sample after 10-h BM and 45 min sintering at 1000°C resulted in the highest density. Further characterization of the Fe-9Cr alloy has been carried out on the samples produced by the aforementioned process route.

Figure 5 shows the XRD pattern of the SPS sample. The pattern shows the predominance of the ferrite phase (BCC lattice structure).
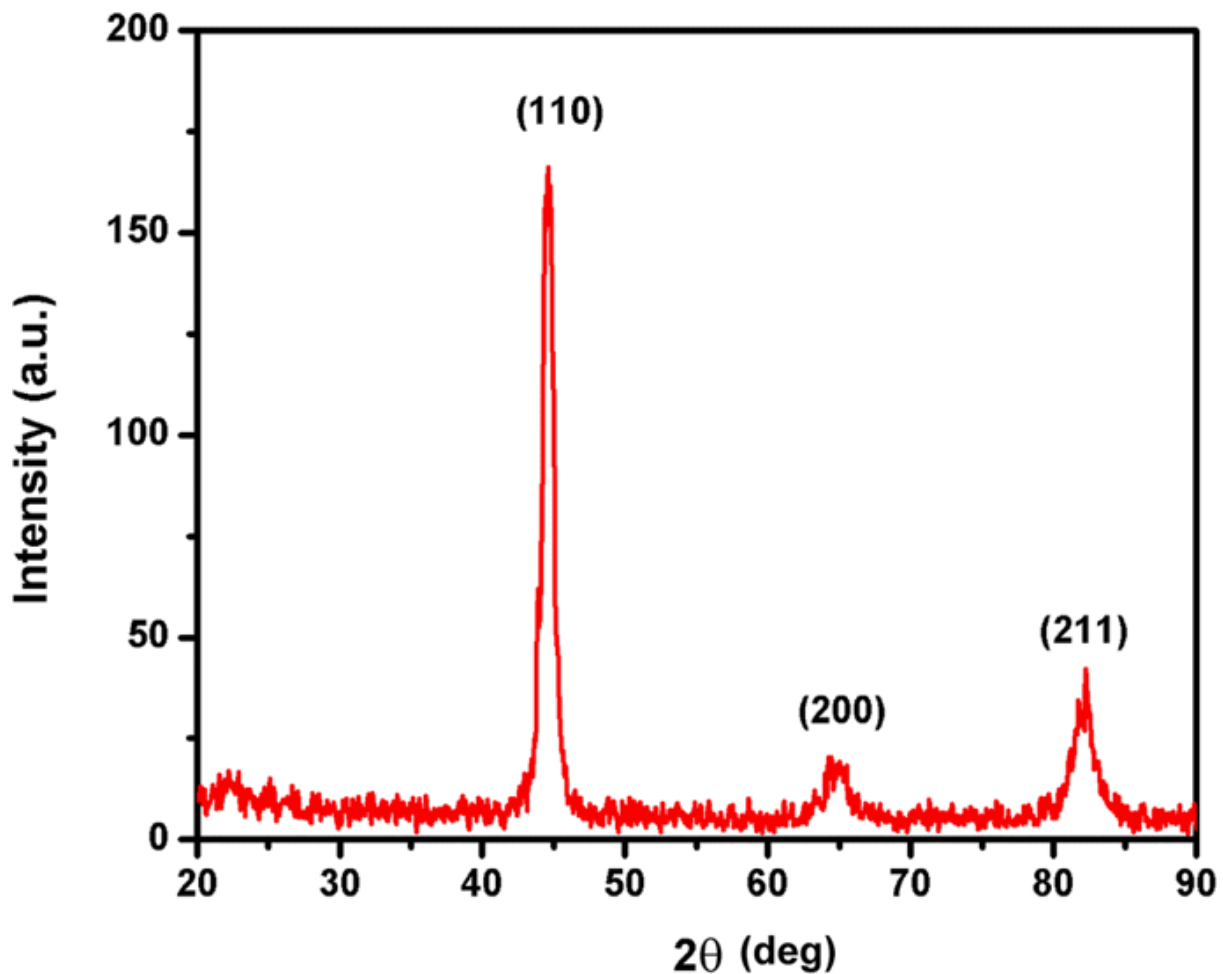

Fig. 5
XRD pattern of the SPS Fe-9Cr sample

Figure 6a shows the inverse pole figure map of the SPS Fe-9Cr alloy. The orientation of the crystal planes is in the normal direction, i.e., the direction of applied pressure during the SPS process. Figure 6b shows the direct pole figures for the three low index family of planes. The

grains are found to be randomly oriented throughout the matrix, which confirms that the SPS imparts a fairly random texture.[33] Figure 6c shows the grain boundary (GB) misorientation map of the sample and Fig. 6d shows the corresponding GB misorientation histogram. Both the figures show that the low-angle GB resolved is only a small fraction of the total grain boundaries. The grain size was found to range from 0.4 μm to about 10 μm, as seen in Fig. 6e. The mean grain size was found to be about 2 μm, which is similar to that measured from the TEM images.
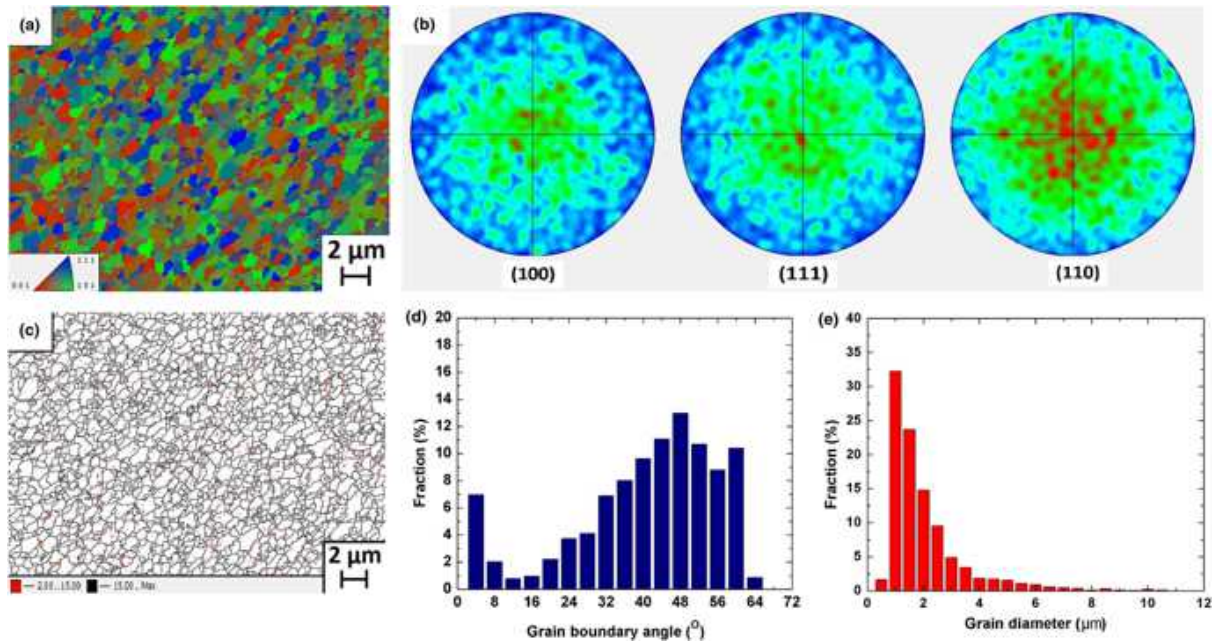

Fig. 6
EBSD results of the SPS (1000°C/45 min) Fe-9Cr: (a) inverse pole figure map, (b) direct pole figures, (c) grain boundary angle map, (d) grain boundary misorientation distribution histogram, and (e) grain size distribution histogram

Evaluation of Compression Properties

The true stress–true plastic strain curve of the SPS Fe-9Cr in compression is shown in Fig. 7, from which it can be seen that the yield stress was determined to be about 642 MPa. Using the well-known Hollomon's equation, the strain-hardening exponent was calculated to be around 0.12.
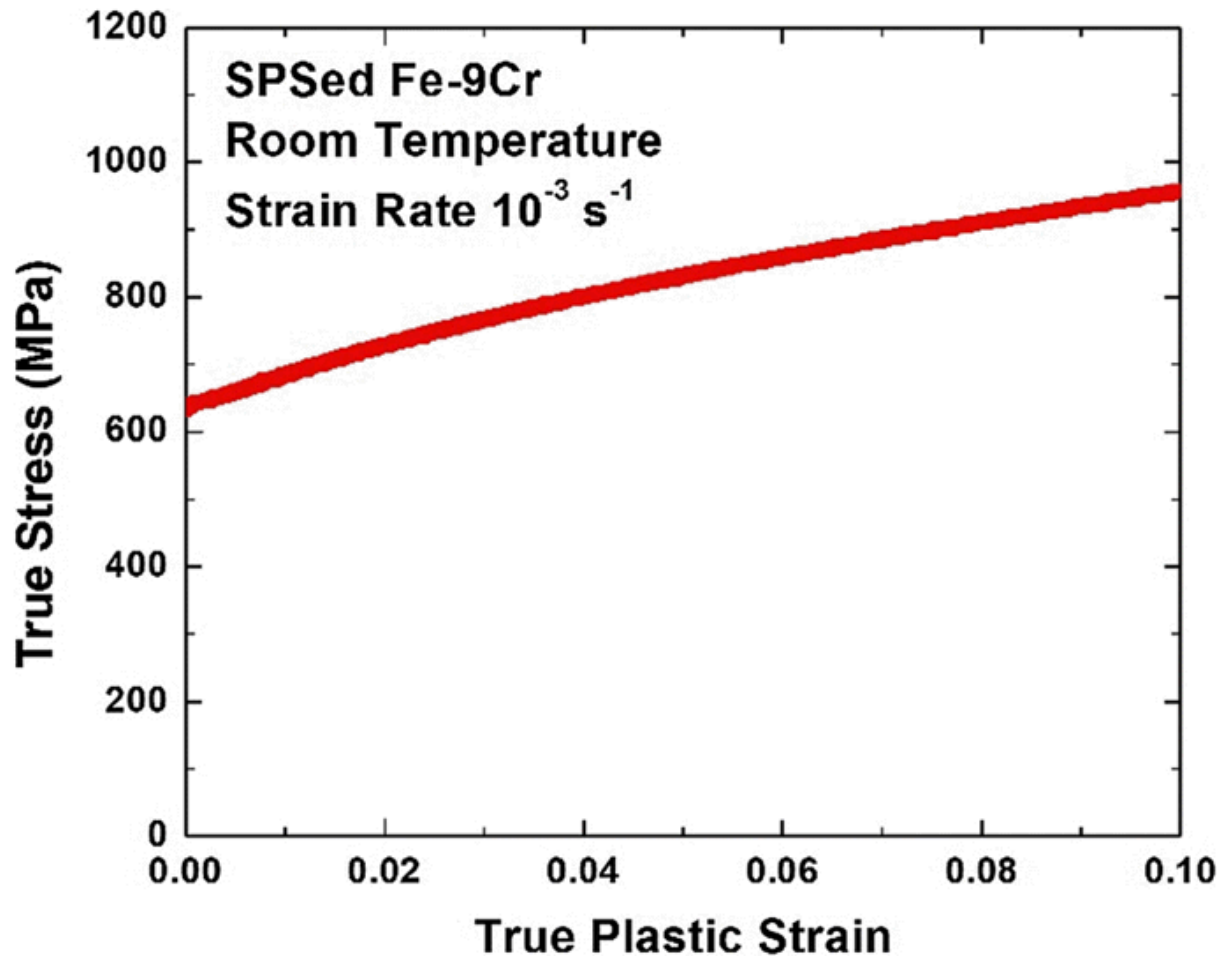
Fig. 7
Compression stress–strain curve (true stress versus true plastic strain) of the Fe-9Cr alloy

Sintering Kinetics

In order to understand the SPS kinetics, the model proposed by Young and Cutler[34] has been used. In their study, non-isothermal equations for volume and GB diffusion have been modified. The equations represent the relationship between the shrinkage (Y) and diffusion coefficient (D), where c represents the heating ramp rate in units of Ks−1Ks−1[34]:

$$\ln\left(YT\frac{dY}{dT}\right)=\ln\left(\frac{2.63\gamma\Omega D_{0V}}{ka^3c}\right)-\frac{Q_V}{RT} \tag{2}$$

$$\ln\left(Y^2T\frac{dY}{dT}\right)=\ln\left(\frac{0.71\gamma b\Omega D_{0B}}{ka^4c}\right)-\frac{Q_B}{RT} \tag{3}$$

where Y is the linear shrinkage ($\Delta l/l_0$), Ω is the volume of vacancy (m3), γ is the surface energy (J/m2), DV is the volume diffusion coefficient given by $D_V = D_{V0}\exp(-Q_V/RT)$ (m2 s−1), bDB is the product of the GB thickness 'b' and GB diffusion coefficient 'DB' given by $bD_B = bD_{B0}\exp(-Q_B/RT)$ bDB=bD0Bexp

(−QB/RT) (m3 s−1), k is the Boltzmann constant (J/K), T is the temperature (K), a is the particle radius (m) and t is time (s). QV and QB are the activation energies for volume diffusion and GB diffusion, respectively. The activation energies for volume diffusion and GB diffusion can be obtained from the slope of the plots between ln (YT(dY/dT)) versus 1/T and ln (Y2T(dY/dT)) versus 1/T, respectively.

Figure 8a depicts the displacement profile curve of the SPS sample. A constant heating rate has been used during the SPS process. The temperature at which densification begins (Ts) and the temperature at which maximum densification rate occurs (Tmax) are calculated from the displacement curve and its first derivative, respectively.[35] It has been found that densification starts around 600°C and reaches the maximum rate at 825°C which is similar to the values obtained by previous studies.[36]

Fig. 8
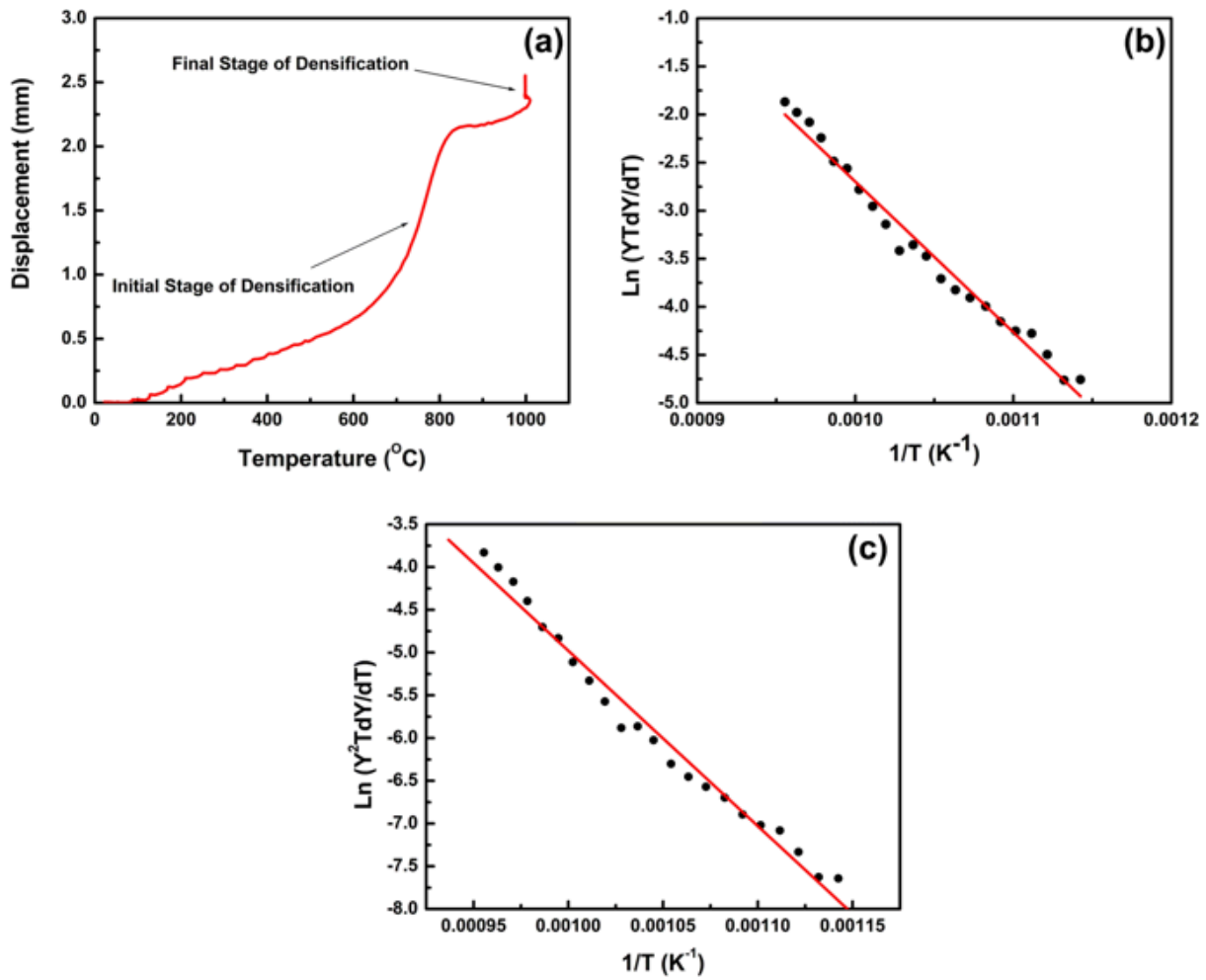
(a) Displacement profile curve of the SPS Fe-9Cr. Activation energy plots for (b) volume diffusion and (c) grain boundary diffusion

From the slope of the ln(YT dY/dT) versus 1/T plots shown in Fig. 8b, the volume diffusion activation energy for the alloy was estimated to be 130 ± 3 kJ/mol. From the slope of the ln(Y2T dY/dT) versus 1/T plots shown in Fig. 8c, the GB diffusion activation energy for the alloy was estimated to be 170 ± 6 kJ/mol. The activation energies for volume diffusion and GB diffusion of pure α-Fe are 251 kJ/mol and 174 kJ/mol, respectively.[37] The nanograin boundary diffusion for Fe powder was estimated by Lee et al.[38] to be 187 kJ/mol.

Thus, in the initial phase of sintering, i.e., from 600°C to 850°C, the GB diffusion is found to be the dominant mechanism. The plausible reason for this could be the preponderance of boundaries due to the nanocrystalline crystallite size produced during BM. However, during SPS, various mechanisms can occur, as reported in previous studies.[15] In the initial phase, surface diffusion is the dominant mechanism because the electric charge is concentrated mainly on the outer surface of the particles, leading to a capacitive nature between two nearby particles, thus producing enough heat for the surface diffusion to take place. In the later stage, when enough particles have fused together, the volume diffusion might come into play, as depicted in Fig. 8a. However, the exact mechanism of the final stage of densification is as yet unknown.

Analysis of Strengthening Mechanisms

While there are different formalisms of predicting yield strength (σ_y) considering superposition of individual strengthening mechanisms, σ_y is expressed using a linear summation relationship[39]:

$$\sigma_y = \sigma_{P-N} + \sigma_{SS} + \sigma_{GB} + \sigma_P + \sigma_D$$

$$(4)$$

where σ_{P-N} is the friction stress (Peierls–Nabarro stress), σ_{SS} is the solid solution strengthening, σ_{GB} is the GB strengthening, σ_P is the precipitation strengthening and σ_D is the dislocation strengthening. Another way of expressing σ_y is based on the assumption that the obstacle strengths for dislocation strengthening and particle strengthening are of similar magnitude, and hence a non-linear additivity rule, as shown in Eq. 5.[40]

$$\sigma_y = \sigma_{P-N} + \sigma_{SS} + \sigma_{GB} + \sqrt{\sigma_P^2 + \sigma_D^2}$$

$$(5)$$

In this study, the value of σ_{P-N} for pure iron is taken as 50 MPa.[41] The value of σ_{SS} is calculated using the following equation[42]:

$$\sigma_{SS} = \sum A_i C_i$$

(6)

where A_i is the strengthening coefficient of alloying elements: C (5544 MPa/wt.%)[43] and Cr (8.5 MPa/wt.%).[44] C_i is the wt.% of the alloying elements.

The value of σ_{GB} is calculated using the Hall–Petch equation:[41]

$$\sigma_{GB} = kd^{-\frac{1}{2}}$$

(7)

where k is a constant (310 MPa $\mu m^{1/2}$)[41] and d is average grain diameter as calculated (2 μm).

The value of σ_P is calculated using the Orowan–Ashby equation:[45]

$$\sigma_p = 0.538 \, Gb \frac{\sqrt{f}}{d_p} \ln\left(\frac{d_p}{2b}\right)$$

(8)

where G is the shear modulus of iron (60 GPa), b is the Burgers vector (0.248 nm), f is the volume fraction of the chromium oxide particles (0.05) and dp is the average particle diameter (0.1 μm).

The strengthening (σ_D) due to the dislocation density is obtained by the following equation[46]:

$$\sigma_D = \alpha M G b \sqrt{\rho}$$

(9)

where α is a numerical constant which is usually taken as 0.3–0.6, M Taylor's factor (2.78 for BCC), G is the shear modulus, b the Burgers vector, and ρ the dislocation density (0.89 × 10^{14} m^{-2}) as evaluated using the following equation[47,48]:

$$\rho = \frac{2\sqrt{3} \langle \xi^2 \rangle^{0.5}}{d \times b}$$

(10)

where $\langle \xi^2 \rangle^{0.5}$ is the mean lattice strain (0.013%) obtained from the XRD pattern (by the Williamson–Hall method) of sintered specimens; d and b have already been defined.

The predicted yield strength values are included in Table II alongside the estimated individual strengthening mechanism contributions. The predicted yield strength from the linear superposition rule came to be around 651 MPa, which is closer to the experimentally

determined value (642 MPa), while the non-linear superposition resulted in a yield strength value of 594 MPa.

Table II. Comparison of predicted yield strength and experimental yield strength for the SPS Fe-9Cr alloy

	σ_{P-N} (MPa)	σ_{SS} (MPa)	σ_{GB} (MPa)	σ_p (MPa)	σ_D (MPa)	Predicted σ_y— Eq. 4 (MPa)	Predicted σ_y— Eq. 5 (MPa)	Calculated σ_y— experimental (MPa)
Strengthening mechanisms	50	187	219	94	101	651	594	642

Previously, Fe-9Cr alloys have been made via casting.[49,50,51] The cast structures had microhardness of about 390 VHN, although it had a martensitic structure with precipitates of MX, M23C6, Laves phase, and Z phase. But due to the very small grain size of the sintered sample compared to that of the cast sample (around 20 µm), the hardness was higher than that of the cast alloy. Large elongated segregations of Cr-rich phases have been seen in those alloys.[52] However, after consolidation by SPS, we could not find any such martensitic structure as the material under study has a very low carbon content. EDS analysis has been carried out on various regions of the consolidated sample, but no Cr-rich segregations have been found. Fe-9Cr ODS steel has also been prepared by the BM process and, for 10-h and 20-h BM times, the mean powder size is close to what we achieved, as reported by Xu et al.[53] Heintze et al. [23] reported that Fe-9Cr ODS produced by a combined process of BM, SPS and HIP had a relative density level of 98.1%, which is quite close to the 97.9% that we obtained by BM and SPS.

Conclusion

The main objective of this study was to develop a fabrication route for the Fe-9Cr model alloy. This work involved optimization of the BM and SPS parameters.

1. The high-energy ball-milling of Fe-9Cr samples for longer durations resulted in decreased powder size and nanocrystalline crystallite size in the milled powder.
2. With increasing milling time, the powder size decreased and the powder size distribution also became narrower. The lattice parameter showed only slight variation with changes in BM time.
3. During SPS with increasing sintering temperature, the diffusion process increased, but at a higher temperature the densification process became almost constant. A BM time of 10 h, SPS temperature of 1000°C and sintering time of 45 min have been found to be optimum for producing the Fe-9Cr alloy.

4. TEM analysis revealed the presence of Cr-based fine oxide particles in the matrix, which adds to the high hardness of the material due to particle hardening.

5. EBSD analysis showed no preferred texture throughout the alloy.

6. A kinetics study indicates that, in the initial stage of SPS, GB diffusion is the dominant mechanism for the consolidation process.

7. Analysis of strengthening mechanisms using a linear superposition revealed the best correlation between the predicted yield strength and the experimentally obtained yield strength.

Acknowledgement

References

1. Kohyama, A. Hishinuma, D.S. Gelles, R.L. Klueh, W. Diets, and K. Ehrich, J. Nucl. Mater. 138, 233 (1996).

2. F.A. Garner, M.B. Toloczko, and B.H. Sencer, J. Nucl. Mater. 276, 123 (2000).

3. R.L. Klueh and D.H. Harries, High-Chromium Ferritic and Martensitic Steels for Nuclear Applications, Vol. 3 (West Conshohocken: ASTM International, 2001).

4. Raj, S.L. Mannan, P. Rao, and M.D. Mathew, Sadhana 7, 527 (2002).

5. Suryanarayana, Prog. Mater Sci. 46, 1 (2001).

6. C.L. Chen and Y.M. Dong, Mater. Sci. Eng. A 528, 8374 (2011).

7. Suryanarayana, E. Ivanov, and V.V. Boldyrev, Mater. Sci. Eng. A 304, 151 (2001).

8. J.B. Fogagnolo, F. Velasco, M.H. Robert, and J.M. Torralba, Mater.

9. M. Zawrah and L. Shaw, Mater. Sci. Eng. A 355, 37 (2003).

10. R. Juarez, J.J. Sunol, R. Berlanga, J. Bonastre, and L. Escoda, J. Alloys Compd. 434, 472 (2007).

11. Z. Oksiuta and N. Baluc, J. Nucl. Mater. 386, 426 (2009).

12. H.J. Fecht, Nanostruct. Mater. 6, 33 (1995).

13. O. Guillon, J. Gonzalez-Julian, B. Dargatz, T. Kessel, G. Schierning, J. Rathel, and M. Herrmann, Adv. Eng. Mater. 16, 830 (2014).

14. KU Leuven, SPS Process Modeling (KU Leuven Department of Materials Engineering). https://www.mtm.kuleuven.be/Onderzoek/Ceramics/research/sintering/spark-plasma. Accessed 27 Sept 2018.

15.   M. Suárez, A. Fernández, J.L. Menéndez, R. Torrecillas, H. U. Kessel, J. Hennicke, R. Kirchner, and T. Kessel, Challenges and Opportunities for Spark Plasma Sintering: A Key Technology for a New Generation of Materials in Sintering Applications (Burcu Ertuğ, IntechOpen, 2013). http://dx.doi.org/10.5772/53706. Accessed 27th Sept 2018.

16.   R. Orru, R. Licheri, A.M. Locci, A. Cincotti, and G. Cao, Mater. Sci. Eng. R 63, 127 (2009).

17.   Olevsky, S.Y. Kandukuri, and L. Froyen, J. Appl. Phys. 102, 114913 (2007).

18.   L. Toualbi, C. Cayron, P. Olier, J. Malaplate, M. Praud, M.-H. Mathon, D. Bossu, E. Rouesne, A. Montani, R. Logé, and Y. de Carlan, J. Nucl. Mater. 428, 47 (2012).

19.   S. Noh, A. Kimura, and T.K. Kim, Fusion Eng. Des. 89, 1746 (2014).

20.   S.A. Briggs, P.D. Edmondson, K.C. Littrell, Y. Yamamoto, R.H. Howard, C.R. Daily, K.A. Terrani, K. Sridharan, and K.G. Field, Acta Mater. 129, 217 (2017).

21.   S. Li, Y. Wang, X. Dai, F. Liu, J. Li, and X. Wang, J. Nucl. Mater. 478, 50 (2016).

22.   K. Ono, K. Arakawa, H. Shibasaki, H. Kurata, I. Nakamichi, and N. Yoshida, J. Nucl. Mater. 329, 933 (2004).

23.   C. Heintze, M. Hernandez-Mayoral, A. Ulbricht, F. Bergner, A. Shariq, T. Weissgarber, and H. Frelinghaus, J. Nucl. Mater. 428, 139 (2012).

24.   M. Zakeri and A. Nazari, Neural Comput. Appl. 21, S723 (2012).

25.   J.B. Nelson and D.P. Riley, Proc. Phys. Soc. 57, 160 (1945).

26.   G.K. Williamson and W.H. Hall, Acta Metall. 1, 22 (1953).

27.   Y. Zhenhua, X. Weihao, Y. Ming, and P. Qianyun, J. Nucl. Mater. 403, 198 (2010).

28.   S. Pasebani, I. Charit, D.P. Butt, and J.I. Cole, J. Nucl. Mater. 434, 282 (2013).

29.   X.T.A. Chu, B.N. Ta, L.T.H. Ngo, M.H. Do, P.X. Nguyen, and D.N.H. Nam, J. Electron. Mater. 45, 2311 (2016).

30.   R.K. Khatirkar and B.S. Murty, Mater. Chem. Phys. 123, 247 (2010).

31.   A.R. Denton and N.W. Ashcroft, Phys. Rev. A 43, 3161 (1991).

32.   B. Arh and F. Tehovnik, Mater. Technol. 41, 203 (2007).

33.   B. Srinivasarao, K. Oh-ishi, T. Ohkubo, and K. Hono, Acta Mater. 57, 3277 (2009).

34.   W.S. Young and I.B. Cutler, J. Am. Ceram. Soc. 53, 659 (1970).

35.   J. Guyon, A. Hazotte, J.P. Monchoux, and E. Bouzy, Intermetallics 34, 94 (2013).

36.   S. Pasebani, I. Charit, D.P. Butt, J.I. Cole, Y. Wu, and J. Burns, Adv. Eng. Mater. 18, 324 (2016).

37.   H.J. Frost and M.F. Ashby, Fundamental Aspects of Structural Alloy Design (Boston: Springer, 1977).

38.   J.S. Lee, J.P. Choi, and G.Y. Lee, Materials 6, 4046 (2013).

39.   D.R. Lesuer, C.K. Syn, and O.D. Sherby, Mater. Trans. 47, 1508 (2006).

40.   Sittiho, V. Tungala, I. Charit, and R.S. Mishra, J. Nucl. Mater. 509, 435 (2018).

41.   W.C. Leslie, Metall. Trans. 3, 5 (1972).

42.   S. Schmauder and C. Kohler, Mater. Sci. 50, 1238 (2011).

43.   G.E. Totten, L. Xie, and K. Funatani, Handbook of Mechanical Alloy Design (New York: Marcel Dekker, 2003).

44.   J. Wang, W. Yuan, R.S. Mishra, and I. Charit, J. Nucl. Mater. 432, 274 (2013).

45.   M.A. Altuna, A. Iza-Mendia, and I. Gutierrez, Metall. Mater. Trans. A 43, 4571 (2012).

46.   W. Li, H. Xu, X. Sha, J. Meng, W. Wang, C. Kang, X. Zhang, and Z. Wang, Fusion Eng. Des. 137, 71 (2018).

47.   K.G. Raghavendra, A. Dasgupta, and P. Bhaskar, Powder Technol. 287, 190 (2016).

48.   M. Mhadhbi, M. Khitouni, L. Escoda, J.J. Suñol, and M. Dammak, J. Nanomater. 2010, 712407 (2010).

49.   O. Boshko, O. Nakonechna, N. Belyavina, M. Dashevskyi, and S. Revo, Adv. Powder Technol. 28, 964 (2017).

50.   Z. Hou, Study of Precipitation in Martensitic Fe-C-Cr Alloys During Tempering: Experiments and Modelling (Royal Institute of Technology, Stockholm, 2015), https://www.diva-portal.org/smash/get/diva2:866846/FULLTEXT01.pdf. Accessed 27th Sept 2018.

51.   T. Shrestha, S.F. Alsagabi, I. Charit, G.P. Potirniche, and M.V. Glazoff, Metals 5, 131 (2015).

52.   V. Kuksenko, Model Oriented Irradiation Experiments in Fe-Cr Model Alloys, Doctoral Thesis in Materials Science, Université de Rouen, France, 2011.

53.   H. Xu, Z. Lu, D. Wang, and C. Liu, Nucl. Mater. Energy 7, 1 (2016).